

Nematostriction in frustrated two-dimensional Heisenberg models

Olav F. Syljuåsen¹ and Jens Paaske²

¹*Department of Physics, University of Oslo, P. O. Box 1048 Blindern, N-0316 Oslo, Norway*

²*Niels Bohr Institute, University of Copenhagen, 2100 Copenhagen, Denmark*

(Dated: February 17, 2026)

We investigate the nematic phase transition in the Heisenberg J_1 - J_2 -model on square and triangular lattices, accounting for finite lattice compressibility and bond-length-dependent magnetic exchange. Using Nematic Bond Theory, a diagrammatic self-consistent method, we study the *nematostriction* that happens when the onset of nematic order in the spin-system drives a concomitant structural phase transition. We analyze the mechanisms by which the magnetoelastic couplings renormalize the critical temperature and modify the phonon spectrum. The magnetoelastic feedback can also alter fundamentally the nature of the phase transition. Specifically, on the square lattice, the transition shifts from continuous to weakly first-order (discontinuous) beyond a critical magnetoelastic coupling threshold. Conversely, on the triangular lattice, the transition remains discontinuous regardless of coupling strength.

Magnetostriction, the elastic deformation of a crystal during a magnetic phase transition, occurs because the exchange coupling between magnetic moments in an insulator depends on the bond length. In two-dimensional frustrated magnets with continuous symmetry, such a structural transition cannot occur due to the absence of magnetic ordering. Nonetheless, vestigial nematic bond ordering could occur at finite temperatures [1, 2], raising the question if this too is accompanied by a structural phase transition and what the nature of this joint transition is. Such a joint transition has already been established in itinerant electronic systems, for which the influence of a compressible lattice on nematic critical properties is being actively investigated and many interesting and surprising effect have already been uncovered [3–8].

Comparatively little is known about how such *nematostriction* plays out in local-moment magnets. The classical two-dimensional elastic square-lattice J_1 - J_2 Heisenberg model was studied in Ref. [9] using Monte Carlo simulations at relatively large magnetoelastic couplings, revealing a concomitant nematic and structural phase transition, which was shown to be in the Ising model universality class. Here we revisit the same model in the complimentary small coupling regime, which is likely also the most relevant experimental regime, and consider both a square, and a triangular lattice.

In order to study large system sizes, we employ the Nematic Bond Theory (NBT) [10], which we extend to also include lattice vibrations. NBT is a self-consistent diagrammatic method for classical spins that treats the local spin-length constraint using a fluctuating Lagrange-multiplier field. It is an extension of the self-consistent Gaussian approximation (SCGA) [11] allowing for spontaneous breaking of the point-group symmetry via the generation of a symmetry breaking momentum-dependent self-energy term. Although NBT is an approximate diagrammatic method neglecting vertex corrections, and is only strictly valid in the limit of infinitely many spin components, $N_s \rightarrow \infty$, it captures the finite-temperature nematic transition of the J_1 - J_2 model very well already for the physically relevant case of $N_s = 3$.

This method has the advantage over Monte Carlo simulations that larger system sizes can be reached for modest computing times, and the free energy can be computed directly. Furthermore, the absence of statistical errors makes it possible to perform accurate extrapolations to the limit of infinite system size.

As in Ref. [9], we find a single joint nematostrictive phase transition. We find evidence, however, that on the square lattice the phase transition becomes discontinuous for magnetoelastic couplings beyond a threshold which is much smaller than the couplings studied in Ref. [9]. We map out how the critical temperature is altered by the magnetoelastic couplings, and calculate how the nematic order influences the phonon spectrum. In section I we define the model and establish the generalized NBT equations. In section II we present the results of the numerical investigations, and in section III we discuss of our findings.

I. COMPRESSIBLE SQUARE LATTICE J_1 - J_2 HEISENBERG MODEL

The J_1 - J_2 Heisenberg model with a distance-dependent interaction is

$$H_J = \frac{1}{2} \sum_{\vec{r}, \vec{r}', \alpha} J(\vec{r}' - \vec{r}) S_{\vec{r}}^{\alpha} S_{\vec{r}'}^{\alpha}, \quad (1)$$

where the atomic spins are treated classically as unit vectors. The atom positions are denoted $\vec{r} = \vec{R} + \vec{u}_{\vec{R}}$ where \vec{R} is a site on a reference lattice with unit lattice vectors \vec{a}_1 and \vec{a}_2 containing in total $N = N_x^2$ sites, and $\vec{u}_{\vec{R}}$ is a displacement. Expanding about the reference lattice, to first order in the displacements, we find

$$J(\vec{r}' - \vec{r}) \approx J(\vec{c}) + (\vec{u}_{\vec{R}+\vec{c}} - \vec{u}_{\vec{R}}) \cdot \nabla J(\vec{c}) \quad (2)$$

where the vector between interacting spins in the reference lattice is denoted $\vec{c} \equiv \vec{R}' - \vec{R}$. We make the assumption that the exchange couplings J are only functions

of the length $|\vec{r}' - \vec{r}|$, and set $\nabla J(\vec{c}) = g_{\vec{c}} \vec{c}/|\vec{c}|$ where $g_{\vec{c}} = \frac{\partial J}{\partial \vec{r}}|_{|\vec{c}|}$ which we will refer to as the magnetoelastic coupling.

The displacement vector $\vec{u}_{\vec{R}}$ is written in terms of the symmetric elastic deformation tensor $\epsilon^{ij} \equiv \left(\frac{\partial u_i}{\partial r_j} + \frac{\partial u_j}{\partial r_i} \right)/2$, and finite wave vector normal modes $X_{m,\vec{k}}$, which we will term phonons, as

$$u_{\vec{R}}^i = \epsilon^{ij} R^j + \sum_{\vec{k} \neq 0} W_{m,\vec{k}}^i e^{i\vec{k} \cdot \vec{R}} X_{m,\vec{k}}, \quad (3)$$

where repeated latin indices are to be summed over. $X_{m,\vec{k}}$ is the amplitude of phonon mode m at wave vector \vec{k} and causes a displacement proportional to the normal mode eigenvector $W_{m,\vec{k}}$. Acoustic zero modes ($\vec{k} = 0$) are excluded from the second term, as they are accounted for by the (uniform) elastic deformations.

The energy of lattice deformations is

$$H_{latt} = \frac{1}{2} N c_{ij,kl} \epsilon^{ij} \epsilon^{kl} + \frac{1}{2} \sum_{\vec{k} \neq 0} M \omega_{m,\vec{k}}^2 |X_{m,\vec{k}}|^2 \quad (4)$$

where $c_{ij,kl}$ is the elastic stiffness tensor per site, symmetric in its first and second pair of indices, and $\omega_{m,\vec{k}}$ are the phonon frequencies. M is the atom mass, which we will set to unity. The phonon frequencies and associated eigenvectors are found by diagonalizing the dynamical matrix

$$D_{\vec{k}}^{ij} = \frac{1}{NM} \sum_{\vec{r},\vec{r}'} \frac{\partial^2 V_{pot}}{\partial r^i \partial r'^j} e^{-i\vec{k} \cdot (\vec{r} - \vec{r}')}|_{eq}. \quad (5)$$

where V_{pot} is the elastic potential energy of the lattice. The summand is evaluated at the atom equilibrium positions $r_{eq}^i = (\delta^{ij} + \epsilon^{ij}) R^j$ so as to account for a modified phonon spectrum in the uniformly distorted lattice.

We will assume a concrete microscopic model where V_{pot} results from elastic bonds with spring constants $\alpha_1(\alpha_2)$ between first(second) neighbors, and consider only in-plane displacements. For the undistorted square lattice this gives the following dynamical matrix

$$\begin{aligned} D_{\vec{k}}^{xx} &= 2 \frac{\alpha_1}{M} (1 - \cos k_x) + 2 \frac{\alpha_2}{M} (1 - \cos k_x \cos k_y), \\ D_{\vec{k}}^{yy} &= 2 \frac{\alpha_1}{M} (1 - \cos k_y) + 2 \frac{\alpha_2}{M} (1 - \cos k_x \cos k_y), \\ D_{\vec{k}}^{xy} &= 2 \frac{\alpha_2}{M} \sin k_x \sin k_y = D_{\vec{k}}^{yx}, \end{aligned} \quad (6)$$

which yields $N_{ph} = 2$ acoustic phonon branches. The $\vec{k} = 0$ limit of $D_{\vec{k}}^{ij}$ gives the components of the elastic stiffness tensor according to $D_{\vec{k}}^{ik} \sim \frac{1}{M} \sum_{k,l} c_{ij,kl} k^j k^l$, which yields the non-zero components $c_{xx,xx} = c_{yy,yy} = \alpha_1 + \alpha_2$ and $c_{xx,yy} = c_{yy,xx} = c_{xy,xy} = \alpha_2$. These components can be written as a three-by-three matrix in Voigt notation and diagonalized to give independent elastic modes ϵ_n with associated stiffnesses μ_n , $n \in \{1, 2, 3\}$. The orthorhombic

mode $\epsilon_1 = (\epsilon^{xx} - \epsilon^{yy})/\sqrt{2}$ with stiffness $\mu_1 = \alpha_1$ describes elongation in one direction and compression in the other, $\epsilon_2 = \epsilon^{xy} + \epsilon^{yx}$, $\mu_2 = \alpha_2$ describes a shear mode and $\epsilon_3 = (\epsilon^{xx} + \epsilon^{yy})/\sqrt{2}$ with $\mu_3 = \alpha_1 + 2\alpha_2$ is the volumetric mode changing the volume. For concreteness, hereafter we will take $\alpha_1 = 2\alpha_2 = \alpha$, corresponding to an isotropic crystal.

Rewriting the spins and couplings in terms of their Fourier transforms and inserting normal modes and elastic deformations for the displacements, the magnetic Hamiltonian can be written

$$H_J = \sum_{\vec{q},\vec{q}',\alpha} S_{\vec{q}}^{\alpha*} (J_{\vec{q}} \delta_{\vec{q},\vec{q}'} + \epsilon_n g_{n,\vec{q}} \delta_{\vec{q},\vec{q}'} + i \tilde{\Gamma}_{\vec{q},\vec{q}'}^m \tilde{q} \cdot \tilde{q}' X_{m,\vec{q}-\vec{q}'}) S_{\vec{q}'}^{\alpha} \quad (7)$$

where $g_{n,\vec{q}}$ is the linear combination of Fourier-transformed spin-phonon couplings that couples to elastic mode n . Keeping only first and second neighbor spin-phonon couplings $g_1 \equiv g_{\pm \vec{a}_1} = g_{\pm \vec{a}_2}$ and $g_2 \equiv g_{\pm (\vec{a}_1 + \vec{a}_2)} = g_{\pm (\vec{a}_1 - \vec{a}_2)}$ these are

$$\begin{aligned} g_{1,\vec{q}} &= \frac{g_1}{\sqrt{2}} (\cos q_x - \cos q_y), \\ g_{2,\vec{q}} &= -g_2 \sqrt{2} \sin q_x \sin q_y, \\ g_{3,\vec{q}} &= \frac{g_1}{\sqrt{2}} (\cos q_x + \cos q_y) + 2g_2 \cos q_x \cos q_y. \end{aligned} \quad (8)$$

Note that only $g_1(g_2)$ determines the coupling strength to the first(second) elastic mode, while both determine the coupling to the isotropic volume compression mode.

The spin-phonon interaction vertex is

$$\tilde{\Gamma}_{\vec{q},\vec{q}'}^m \tilde{q} \cdot \tilde{q}' = \frac{1}{\sqrt{N}} \sum_{\vec{c}} g_{\vec{c}} e^{i\vec{q}' \cdot \vec{c}} f_{m,\vec{q}-\vec{q}',\vec{c}} \quad (9)$$

with

$$f_{m,\vec{q},\vec{c}} = \frac{1}{2i} \frac{c^j}{|\vec{c}|} W_{m,\vec{q}}^j (e^{i\vec{q} \cdot \vec{c}} - 1). \quad (10)$$

Normal modes with zero momenta are not included here, as they correspond to uniform elastic deformations which are explicitly accounted for by ϵ .

The unit length constraint on the spins is taken into account by delta-functions written as an integral over a constraint field $\lambda_{\vec{R}}$:

$$\prod_{\vec{R}} \delta(|\vec{S}_{\vec{R}}| - 1) = \int \prod_{\vec{R}} \frac{\beta d\lambda_{\vec{R}}}{\pi} e^{-i\beta \lambda_{\vec{R}} (\vec{S}_{\vec{R}} \cdot \vec{S}_{\vec{R}} - 1)}. \quad (11)$$

We will take the Fourier transform of the constraint field. Then the integration over the Fourier component $\lambda_{\vec{q}}$ enforces a constraint on the spatial modulation of squared spin lengths with wave vector \vec{q} . For $\vec{q} \neq 0$ these modulations are enforced to be zero, while for $\vec{q} = 0$ the -1 in the exponent forces the squared spin lengths to add up to N . We will therefore treat $\lambda_{\vec{q}=0}$ separately and write it as $\lambda_{\vec{q}=0} = -i\Delta$ where Δ is a real number.

Then putting everything together, the partition function becomes

$$Z = \int D\Delta D\epsilon D\lambda DXDS e^{-S} \quad (12)$$

with

$$\begin{aligned} S = \sum_{\vec{q}, \vec{q}', \alpha} S_{\vec{q}}^{\alpha*} & \left[(J_{\vec{q}} + \Delta + \epsilon_n g_{n, \vec{q}}) \delta_{\vec{q}, \vec{q}'} \right. \\ & \left. - (-i) \left(\tilde{\Gamma}_{\vec{q}, \vec{q}'}^{m \vec{q} - \vec{q}'} X_{m, \vec{q} - \vec{q}'} + \lambda_{\vec{q} - \vec{q}'} \right) \right] S_{\vec{q}'}^{\alpha} \\ & - \beta N \Delta + \frac{\beta N}{2} \mu_n \epsilon_n^2 + \frac{\beta}{2} \sum_{\vec{k}, m} M \omega_{m, \vec{k}}^2 |X_{m, \vec{k}}|^2 \end{aligned} \quad (13)$$

and the spins have been rescaled by a factor $\sqrt{\beta}$.

The bare inverse spin propagator can be written as a matrix \mathbf{K} diagonal in \vec{q} -space

$$K_{\vec{q}\vec{q}'} = K_{\vec{q}} \delta_{\vec{q}, \vec{q}'}, \quad K_{\vec{q}} \equiv (J_{\vec{q}} + \Delta + \epsilon_n g_{n, \vec{q}}). \quad (14)$$

The form of Eq. (13) makes it convenient to define a combined constraint and phonon field $Y_{m, \vec{q}}$ in the following way

$$Y_{m, \vec{q}} = \begin{cases} \lambda_{\vec{q}}, & m = 0 \\ X_{m, \vec{q}}, & m \in [1, N_{\text{ph}}] \end{cases} \quad (15)$$

where the index m takes integer values starting from 0, so that the constraint field is the zeroth component. $N_{\text{ph}} = 2$ is the number of phonons modes. With this combined field the coupling to the spins can be written as a matrix $\mathbf{\Lambda}$ with matrix elements

$$\Lambda_{\vec{q}\vec{q}'} = (-i) \Gamma_{\vec{q}, \vec{q}'}^{m \vec{q} - \vec{q}'} Y_{m, \vec{q} - \vec{q}'} \quad (16)$$

where the vertex function is

$$\Gamma_{\vec{q}, \vec{q}'}^{m \vec{q} - \vec{q}'} = \begin{cases} 1, & m = 0, \\ \tilde{\Gamma}_{\vec{q}, \vec{q}'}^{m \vec{q} - \vec{q}'} & m \in [1, N_{\text{ph}}]. \end{cases} \quad (17)$$

Generalizing the number of spin components to N_s and integrating over the spins we arrive at the following expression for the partition function

$$Z = C \int D\Delta D\epsilon DY e^{-(S_0 + S_2 + S_r)} \quad (18)$$

where we have factored out the field-independent constants C , and divided the remainder into terms according to their powers of Y so that

$$S_0 = -\beta N \Delta + \frac{\beta N}{2} \mu_n \epsilon_n^2 + \frac{N_s}{2} \text{Tr} \ln \mathbf{K}, \quad (19)$$

$$S_2 = -\frac{N_s}{2 \cdot 2} \text{Tr} (\mathbf{K}^{-1} \mathbf{\Lambda} \mathbf{K}^{-1} \mathbf{\Lambda}) + \frac{\beta}{2} \sum_{\vec{q}, m=1}^{N_{\text{ph}}} M \omega_{m, \vec{q}}^2 |Y_{m, \vec{q}}|^2$$

$$\equiv \frac{1}{2} \mathbf{Y}^\dagger \mathbf{D}^{-1} \mathbf{Y} \quad (20)$$

$$S_r = - \sum_{l=3}^{\infty} \frac{N_s}{2 \cdot l} \text{Tr} (\mathbf{K}^{-1} \mathbf{\Lambda})^l. \quad (21)$$

The functional integral over Y is then carried out approximately by constructing a diagrammatic theory where K^{-1} refers to the spin-spin correlation function with denominator

$$K_{\vec{q}} = J_{\vec{q}} + \Delta + \epsilon_n g_{n, \vec{q}} + \Sigma_{\vec{q}}, \quad (22)$$

and Gaussian averages with respect to S_2 constitute the inverse constraint-phonon field propagator,

$$\begin{aligned} D_{\vec{q}}^{-1 m m'} &= \beta M \omega_{m, \vec{q}}^2 \delta_{m' m} (1 - \delta_{m, 0}) \\ &+ \frac{N_s}{2} \sum_{\vec{k}} K_{\vec{k}}^{-1} \Gamma_{\vec{k}, \vec{k} + \vec{q}}^{m \vec{q} - \vec{q}'} K_{\vec{k} + \vec{q}}^{-1} \Gamma_{\vec{k} + \vec{q}, \vec{k}}^{m' \vec{q}}. \end{aligned} \quad (23)$$

It should be noted, that the different components of the Y -field in Eq. (15), and of the vertex function in Eq. (17), and therefore for the constraint-phonon field propagator have different dimensions. With this extension to include the phonons, the self-consistent diagrammatic approximation follows the NBT approach detailed earlier in Refs. [10, 12]. The spin-spin correlation function is dressed with the Fock self-energy,

$$\Sigma_{\vec{k}} = \sum_{\vec{q}} \Gamma_{\vec{k}, \vec{k} + \vec{q}}^{m \vec{q} - \vec{q}'} K_{\vec{k} + \vec{q}}^{-1} \Gamma_{\vec{k} + \vec{q}, \vec{k}}^{m' \vec{q}} D_{\vec{q}}^{m' m}, \quad (24)$$

calculated with fully dressed propagators, but leaving out vertex corrections. Approximating the integral over Y as rings of diagrams without vertex and other $\mathcal{O}(1/N_s)$ corrections, see Ref. [12], the partition function becomes

$$Z = C' \int D\Delta D\epsilon e^{-S'} \quad (25)$$

where

$$\begin{aligned} S' &= -\beta N \Delta + \frac{\beta N}{2} \mu_n \epsilon_n^2 + \frac{N_s}{2} \sum_{\vec{q}} \ln K_{\vec{q}} \\ &+ \frac{1}{2} \sum_{\vec{q} \neq 0} \ln \det D_{\vec{q}}^{-1} - \frac{N_s}{2} \sum_{\vec{q}} (K_{\vec{q}}^{-1} \Sigma_{\vec{q}}). \end{aligned}$$

The remaining integrals are performed using the saddle-point method. The saddle-point equations $\frac{\partial S}{\partial \Delta} = 0$ and $\frac{\partial S}{\partial \epsilon_n} = 0$ yield equations for β and ϵ_n :

$$\beta = \frac{N_s}{2N} \sum_{\vec{q}} K_{\vec{q}}^{-1}, \quad (26)$$

$$\beta \epsilon_n = -\frac{N_s}{2\mu_n N} \sum_{\vec{q}} K_{\vec{q}}^{-1} g_{n, \vec{q}}. \quad (27)$$

(no sum over n). We solve the self-consistent equations numerically by iteration. First, starting values of $\Delta, \beta, \epsilon_n$ and random values for $\Sigma_{\vec{q}}$ are selected. Then these are employed to construct the dynamical matrix, $K_{\vec{q}}^{-1}$, $D_{\vec{q}}$ and a new $\Sigma_{\vec{q}}$. To ensure that critical behavior can be reached, Δ is renormalized by subtracting the minimal value of $\Sigma_{\vec{q}}$, referred to as $\Sigma_{\vec{q}^*}$, thus replacing

$\Delta \rightarrow \Delta - \Sigma_{\vec{q}}^*$. Next, β is calculated using Eq. (26), and ϵ_n using Eq. (27). These values are then used in the next iteration to construct the dynamical matrix, $K_{\vec{q}}^{-1}$, $D_{\vec{q}}$ and $\Sigma_{\vec{q}}$ again. This is repeated until β and ϵ_n converge. After reaching convergence, we calculate the Gibbs free energy per spin at zero external pressure as follows

$$\begin{aligned} \frac{G}{N} = & -\Delta + \frac{1}{2}\mu_n\epsilon_n^2 + \frac{N_s}{2\beta N} \sum_{\vec{q}} \ln(\beta K_{\vec{q}}) \\ & + \frac{1}{2\beta N} \sum_{\vec{q}} \ln(\beta^{-2} \det D_{\vec{q}}^{-1}) - \frac{N_s}{2\beta N} \sum_{\vec{q}} (K_{\vec{q}}^{-1} \Sigma_{\vec{q}}) \\ & - \frac{1}{2\beta} [\ln N + (N_s - 2) \ln \pi + (1 + N_{\text{ph}}) \ln(2\pi)] \end{aligned} \quad (28)$$

where Δ denotes the renormalized value. This expression reduces to the free energy obtained in Ref. [12] when taking $N_{\text{ph}} = 0$ and $\epsilon_n = 0$.

II. RESULTS

A. Square lattice

For the square lattice, we consider first and second neighbor interactions. The corresponding Fourier-transformed interaction reads

$$J_{\vec{q}} = J_1 (\cos q_x + \cos q_y) + 2J_2 \cos q_x \cos q_y.$$

We will focus on the parameter values $J_1 = -1$ and $J_2 > 1/2$ for which $J_{\vec{q}}$ is minimal at $(\pi, 0)$ and $(0, \pi)$. One then expects a point-group symmetry breaking phase transition of the Ising-type which selects between these two minima as the temperature is lowered [1]. As J_2 is reduced towards 0.5, the minima of $J_{\vec{q}}$ become more and more shallow and finally connect the X - and Y -points on the edge of the Brillouin zone along a line-degeneracy to the new minimum at the Γ -point for $J_2 < 1/2$.

1. Critical temperature for zero magnetoelastic coupling

We begin by calculating Gibbs free energy per site for the case when the magnetoelastic couplings are zero and $J_2 = 1$. The result is shown in Fig. 1. It reveals two branches. The low-temperature branch is obtained by starting with a low value of Δ and first picking a random self-energy. The Eqs. (23)-(24) and (26)-(27) are iterated until convergence, and the temperature and free energy are obtained from Eqs. (26) and (28) respectively. Then Δ is increased, but now the converged self-energy from the previous run is used as input instead of a random one. This is repeated to produce the low-temperature branch. At a certain value of Δ the low-temperature branch ends abruptly, and the iterations converge to a point on the high-temperature branch at another temperature. Increasing Δ further traces out the high temperature branch. One can also start by decreasing Δ from

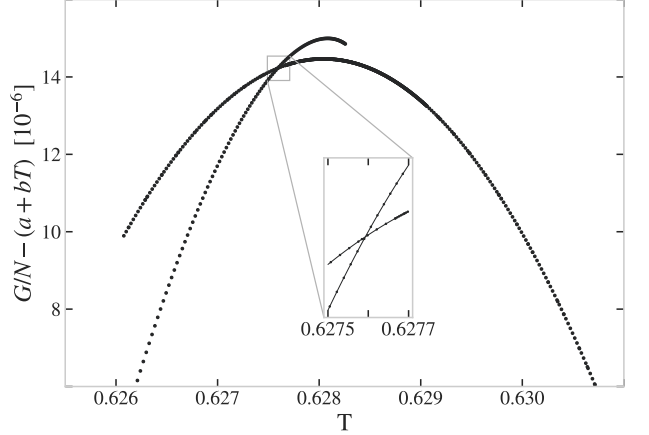


FIG. 1. Gibbs free energy per site vs. temperature for $J_2 = 1$ and zero magnetoelastic coupling. $N_x = 256$. A linear function $a + bT$ with $a = 0.7353$ and $b = -1.65029$ has been subtracted from G/N in order to better visualize the crossing of the two branches at T_c .

a high value. This produces the high-temperature branch that continues until it also ends abruptly and subsequent iterations converge to the low-temperature branch. The branches cross at the phase transition temperature T_c . The discontinuity of slopes at T_c indicates a first order (discontinuous) phase transition. However, this is a finite size effect. As will be shown later in Fig. 5, the discontinuity disappears when $N_x \rightarrow \infty$ for zero magnetoelastic couplings. In Fig. 2, the black circles show how T_c changes as J_2 is varied.

2. Critical temperature for finite magnetoelastic coupling

Next, we investigate finite magnetoelastic couplings. In order to scale out the dependence on the lattice stiffness α , we transform $X_{m, \vec{k}} \rightarrow X_{m, \vec{k}} / \sqrt{\alpha}$ and $\epsilon \rightarrow \epsilon / \sqrt{\alpha}$. This causes the system to depend on the magnetoelastic couplings and lattice stiffness as the combinations $\tilde{g}_i \equiv g_i / \sqrt{\alpha}$, which are the variables we will use in the following. We investigate two sets of magnetoelastic couplings. One with distance-dependent nearest neighbor couplings alone $(\tilde{g}_1, \tilde{g}_2) = (0.1, 0)$ and one with both nearest, and second neighbor distance-dependent couplings $(\tilde{g}_1, \tilde{g}_2) = (0.1, -0.1J_2 / \sqrt{2})$. The inset of Fig. 2 shows how the phase transition temperatures deviate from T_c for zero magnetoelastic couplings. As can be seen, these particular values of \tilde{g} give a substantial relative increase in T_c close to $J_2 = 1/2$ where T_c is already low. For higher values of J_2 the relative change in T_c goes rapidly below the one percent level.

In Fig. 3, we display the more detailed behavior of the nematic T_c on the strength of the magnetoelastic coupling, focusing on two different parameter values, $J_2 = 1$ and $J_2 = 0.51$, for which the inset of Fig. 2 indicates

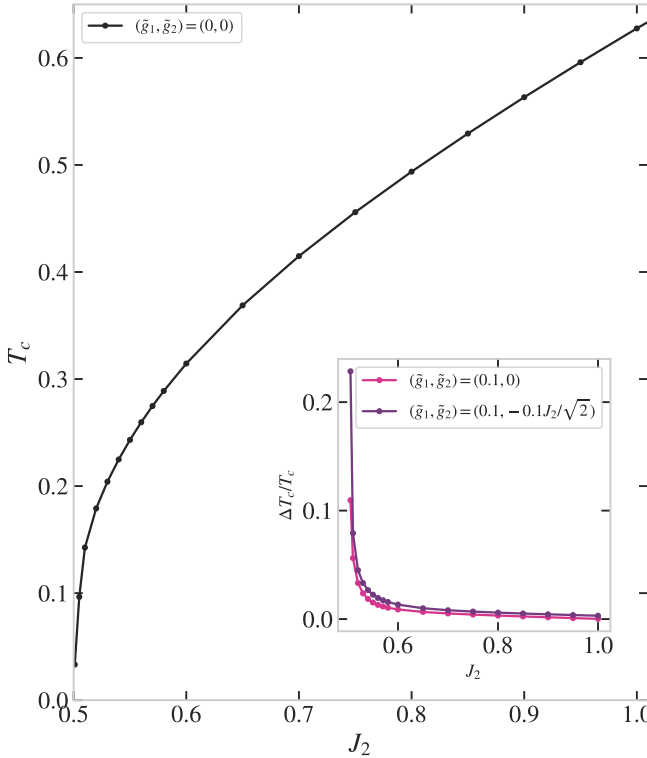


FIG. 2. Main panel: Critical temperature as a function of J_2 for zero magnetoelastic couplings. $N_x = 256$. Inset: Relative change in critical temperatures, $\Delta T_c / T_c \equiv (T_c(\tilde{g}) - T_c(0)) / T_c(0)$, for two sets of magnetoelastic couplings indicated by the legends.

markedly different values of $\Delta T_c / T_c$. Setting $\tilde{g}_2 = 0$ we plot in Fig. 3 T_c as a function of \tilde{g}_1 up to the largest possible values for which convergence could be achieved. The black circles show the full result, which reveals a largely \tilde{g}_1 independent behavior for $J_2 = 1$ and a nearly quadratic increase with \tilde{g}_1 for $J_2 = 0.51$. In order to disentangle the mechanisms that lead to these behaviors, we have solved the self-consistent equations under various simplified conditions, corresponding to the different colored curves in Fig. 3.

First, we perform a minimal calculation in which we leave out the self-energy ($\Sigma = 0$), corresponding to the SCGA, and switch off both shear and volumetric strain ($\epsilon_{2,3} = 0$). The SCGA by itself does not permit breaking of the point-group symmetry, but it is inherently unstable in the sense that any infinitesimal magnetoelastic coupling to orthorhombic strain, ϵ_1 , will allow for the symmetry breaking in much the same manner as a finite self-energy. Even without magnetoelastic coupling, the SCGA already encodes the correct value of T_c , as the crossover temperature below which the solution of Eq. (26), $\Delta(T)$, vanishes exponentially with temperature and may be interpreted as an inverse squared magnetic correlation length. As observed from the purple dots, this crossover temperature becomes a bonafide nematicoelastic

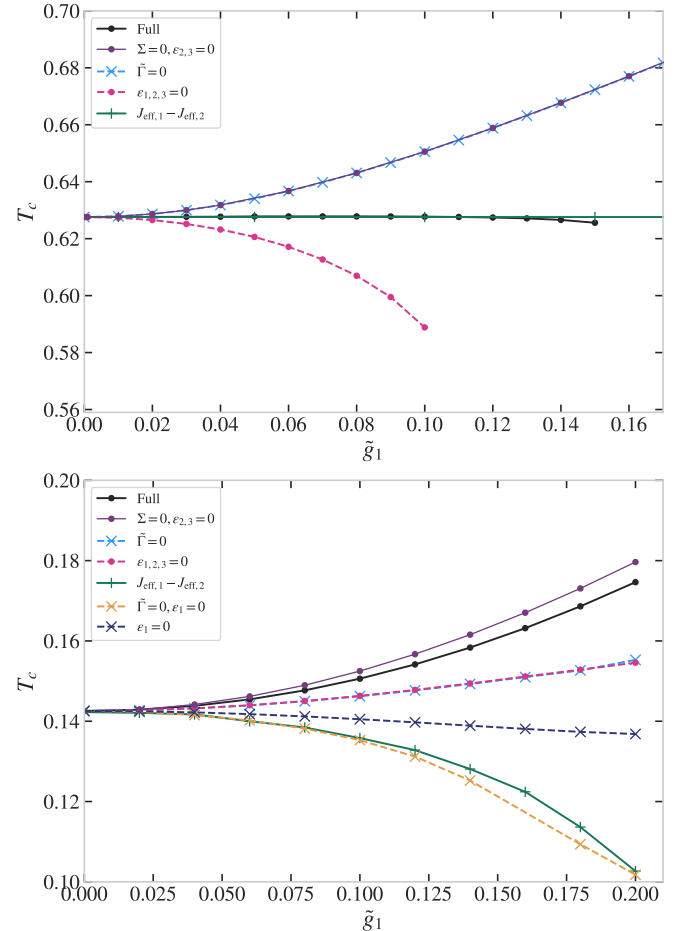


FIG. 3. Critical temperatures T_c vs. \tilde{g}_1 for $J_2 = 1$ (top panel) and $J_2 = 0.51$ (bottom panel), with $\tilde{g}_2 = 0$ and $N_x = 256$. The different curves show results obtained under different conditions imposed on the self-consistent equations as indicated by the legends. Full means no extra conditions.

critical temperature which increases with \tilde{g}_1 in a nearly quadratic manner.

Second, we revert to the full solution, while either leaving out the phonons ($\Gamma = 0$, blue crosses) or clamping the system, i.e. fixing all boundary atoms so as to prohibit any uniform elastic deformations ($\epsilon_{1,2,3} = 0$, pink dots). For $J_2 = 1$, leaving out the phonons makes T_c practically identical to the previous (SCGA) case, indicating that the influence of phonons or constraint fluctuations contribute alike to T_c . This is not true for $J_2 = 0.51$, however, where the blue crosses no-longer match the purple. In the latter case, the blue crosses instead match up with the pink dots, implying that leaving out the phonons has the same effect on T_c as clamping the system. For $J_2 = 1$, on the other hand, the pink dots indicate that phonons cause T_c to decrease with increasing magnetoelastic coupling.

Finally, one may ask how T_c changes with magnetoelastic coupling due to a mere change in the inter-atomic

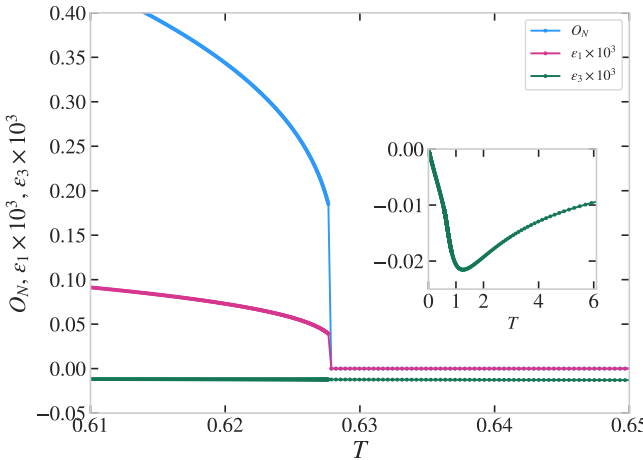


FIG. 4. Order parameters vs. T . Blue curve: Nematic order parameter. Pink curve: Orthorhombic strain ϵ_1 . Green curve: Volumetric strain ϵ_3 . ϵ_1 and ϵ_3 are multiplied by 10^3 . $(\tilde{g}_1, \tilde{g}_2) = (0.03, 0)$, $N_x = 256$. The inset shows $\epsilon_3 \times 10^3$ over a wider temperature range.

distances deriving from a finite volumetric strain, ϵ_3 . For $g_2 = 0$, only J_1 is affected and from Eq. (7) one obtains an effective renormalized exchange coupling of

$$J_{\text{eff},1} = J_1 + g_1 \epsilon_3 / \sqrt{2}. \quad (29)$$

Extracting the values of ϵ_3 from the fully coupled system at a temperature just above T_c and evaluating the renormalized value $J_{\text{eff},1}$, a corresponding value of T_c can be obtained from the formula known from the pure J_1 - J_2 -model with no magnetoelastic coupling, $T_c = |J_1| f_{\square}(J_2/|J_1|)$, where f_{\square} is the curve shown in Fig. 2. The result is shown as the green plusses in Fig. 3. For $J_2 = 1$ this mechanism is seen to have a negligible effect on T_c , deriving from the fact that the function f_{\square} is approximately linear, whereby J_1 cancels from T_c . For $J_2 = 0.51$, on the other hand, the volumetric strain alone leads to a pronounced reduction of T_c with increasing magnetoelastic coupling (cf. green plusses and yellow crosses).

The full equations incorporate all these mechanisms, and we conclude that the almost flat behavior of the black circles for $J_2 = 1$ is caused by a near cancellation of the increasing T_c due to the orthorhombic strain, ϵ_1 , and the decreasing T_c caused by the phonons which takes over for larger values of \tilde{g}_1 . For $J_2 = 0.51$, the volumetric strain, ϵ_3 , alone would lead to a decrease of T_c . However, this decrease is almost fully compensated by the phonons to leave T_c nearly constant (dark blue crosses). Its weak dependence on \tilde{g}_1 indicates that the effects of the phonons and ϵ_3 on T_c almost cancel, and that therefore the full result (black dots) which includes also the rhombohedral strain, ϵ_1 , amounts to a net increase. This explains also the reasonable agreement between the full result (black dots) and the very simplified model with self-energy $\Sigma = 0$ and $\epsilon_{2,3} = 0$ (pink dots).

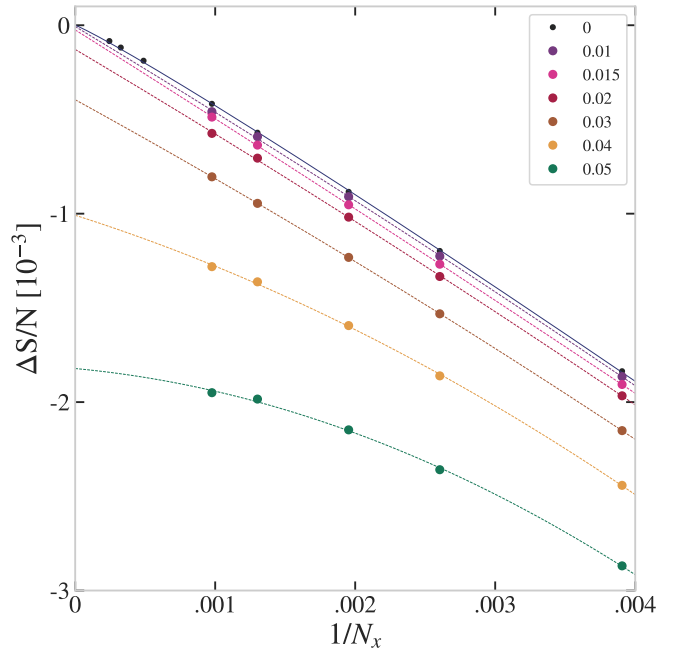


FIG. 5. Entropy discontinuity per spin $\Delta S/N$ vs. inverse linear system size $1/N_x$ at $J_2 = 1$. The black small circles show results for no magnetoelastic couplings ($\tilde{g}_1 = 0$). The colored circles are for different magnetoelastic couplings \tilde{g}_1 as indicated by the legends. $\tilde{g}_2 = 0$.

3. Nature of nematicostrictive phase transition

The phase transition demonstrates *nematicostriction* as the system simultaneously distorts and develops lattice nematic order at T_c . Fig. 4 shows the temperature dependence of both the nematic order parameter, $O_N = \frac{1}{N} \sum_{\vec{r}} \vec{S}_{\vec{r}} \cdot (\vec{S}_{\vec{r}+\hat{x}} - \vec{S}_{\vec{r}+\hat{y}})$, and the symmetry-breaking orthorhombic strain, ϵ_1 , for $\tilde{g}_1 = 0.03$ near the phase transition. The inset shows the temperature dependence of the volumetric strain, ϵ_3 , which has a very small discontinuity of the order 10^{-9} (cf. green dots in main panel) at the transition, near which it attains its maximum (largest negative) value, corresponding to a uniform relative reduction of the order of 10^{-5} .

As seen in Fig. 1 the free energy branches approach the crossing point at T_c with distinct slopes. This indicates a first order phase transition with a small discontinuity in entropy. However, this is a finite size effect as can be seen by extracting the entropy discontinuity for several system sizes. The entropy discontinuity $\Delta S \equiv S(T_c^+) - S(T_c^-)$ is obtained by fitting the free energy branches to quadratic polynomials and computing the difference of their negative temperature derivatives at T_c . For $N_x = 256$ we find $\Delta S/N = -1.8 \cdot 10^{-3}$, and repeating for other system sizes up to $N_x = 4096$ we obtain the values in Fig. 5 shown as small black dots. These values can be fitted to a functional form, $\Delta S = -0.654(1 + 0.05 \log 1/N_x)/N_x$ (solid curve), which tends to zero for $N_x \rightarrow \infty$. We conclude

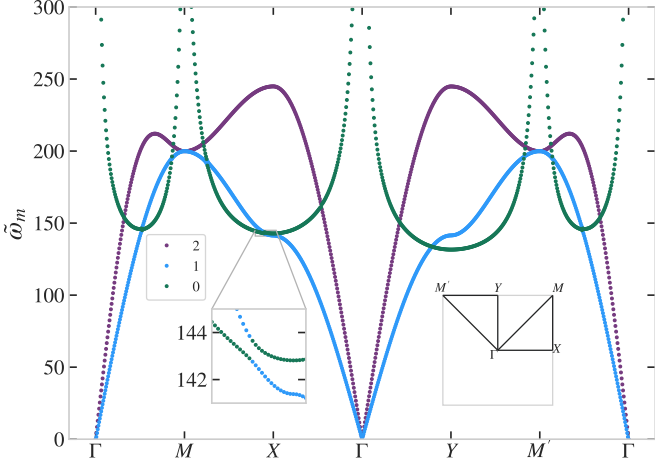


FIG. 6. The renormalized spectra $\tilde{\omega}_{m,\vec{q}}$ for different m values indicated by the legends. The spectra are obtained at $T = 0.604$ just below the phase transition, and is plotted along the Brillouin zone path shown in the right inset. The left inset shows an avoided crossing. $(\tilde{g}_1, \tilde{g}_2) = (0.1, 0)$. $J_2 = 1$, $N_x = 256$.

from this that the phase transition in the absence of magnetoelastic coupling is continuous in the thermodynamic limit $N_x \rightarrow \infty$.

For finite magnetoelastic couplings we also find two branches in the free energy, the crossing of which defines a critical temperature and a discontinuity in entropy, ΔS . The system size dependence of ΔS at the critical temperature is shown as colored symbols in Fig. 5 for different values of \tilde{g}_1 at $J_2 = 1$. For small values of \tilde{g}_1 , ΔS is well fitted by a linear function in $1/N_x$ that extrapolates to very small positive values. This is as for $\tilde{g}_1 = 0$, black dots, if the logarithmic correction is not taken into account. For finite \tilde{g}_1 we are unable to fit the logarithm reliably as system sizes $N_x \gtrsim 1024$ are computationally too demanding when lattice distortions are present. Nevertheless, it is clear that for the largest values of \tilde{g}_1 , the entropy discontinuity will extrapolate to a finite latent heat in the thermodynamic limit and the phase transition is discontinuous.

To estimate the critical value \tilde{g}_{1c} above which the phase transition becomes discontinuous, we fit our finite size points to a second order polynomial and pick the value of \tilde{g}_1 at which it extrapolates to zero. We note that this procedure of determining \tilde{g}_{1c} strictly gives an upper bound as we cannot rule out the possibility of saturation towards a very small but finite negative value for $N_x > 1024$ for smaller \tilde{g} -values. We find $\tilde{g}_{1c} = 0.01$, see Fig. 5. We have also carried out this procedure in the case where the elastic modes are clamped ($\epsilon_{1,2,3} = 0$). We then find practically the same value of \tilde{g}_{1c} . In contrast, for the somewhat artificial case where there are just elastic modes and no phonons, we get $\tilde{g}_{1c}(\Gamma = 0) \approx 0.11$, which is almost an order of magnitude bigger. This implies that the phase transition becomes discontinuous

also in the absence of phonons, and that the presence of phonons alter \tilde{g}_{1c} .

4. Nematic fluctuations: phonons and constraint

The nematic fluctuations also influence the phonon spectrum. The renormalized phonon spectra $\tilde{\omega}_{m,\vec{q}}$ are obtained as the square root of the eigenvalues of D^{-1} multiplied by $\sqrt{T/M}$. This follows from Eq. (23), where the eigenvalues $\tilde{\omega}_{m,\vec{q}}$ are sorted such that the corresponding eigenvector has largest weight on component m . This ensures that the renormalized spectra for $m = 1, 2$ are equal to the bare phonon spectra for zero magnetoelastic coupling. The $m = 0$ component, $\tilde{\omega}_{0,\vec{q}}$, is related to the constraint field. In Fig. 6 we have plotted the renormalized spectra along a path in the Brillouin zone for a temperature just below T_c . The eigenvalues for the renormalized constraint field (green) exhibit a clear XY-asymmetry, while the renormalized phonons (blue and purple) are almost unchanged. However, when plotting the difference between the renormalized and the bare phonon spectra in Fig. 7, one observes marked renormalization both above, and below T_c . This is seen as smooth softenings together with more pronounced sharp features at \vec{q} -points corresponding to the avoided crossings of the $m = 0$ component and the other components in Fig. 6. Clear signs of XY-anisotropy are seen in the two lower panels of Fig. 7, which are obtained below T_c . This rather large anisotropy is caused by the nematic symmetry breaking through the second term in Eq. (23) and is much larger than the elastic deformations, which in this case leads to new lattice vectors $a_x = 1.00024$ and $a_y = 0.99971$ for $T = 0.604$.

B. Triangular lattice

For the triangular lattice we choose lattice vectors $\vec{a}_1 = (1, 0)$ and $\vec{a}_2 = (-1, \sqrt{3})/2$, with associated reciprocal lattice vectors $\vec{b}_1 = (1, 1/\sqrt{3})2\pi$ and $\vec{b}_2 = (0, 2/\sqrt{3})2\pi$. Defining also $\vec{a}_3 \equiv -\vec{a}_1 - \vec{a}_2$, the notation $q_i \equiv \vec{q} \cdot \vec{a}_i$ allows writing the Fourier-transformed exchange coupling as

$$J_{\vec{q}} = J_1 [\cos q_1 + \cos q_2 + \cos q_3] + J_2 [\cos(q_1 - q_2) + \cos(q_2 - q_3) + \cos(q_3 - q_1)]. \quad (30)$$

We consider FM nearest-neighbor exchange, $J_1 = -1$, and AF next-nearest-neighbor exchange, $J_2 > 0$. For $J_2 > 1/3$ the minima of $J_{\vec{q}}$ are located on the $\Gamma - M$ lines in momentum space. These three lines are at a 60° angle with each other (cf. inset in Fig. 9), indicating the three-fold lattice symmetry which can now be spontaneously broken at low temperatures. The spin pattern in the corresponding magnetically ordered phase at zero temperature has spins aligned along one of the three lattice directions, and spins rotating as one moves perpendicular to this direction.

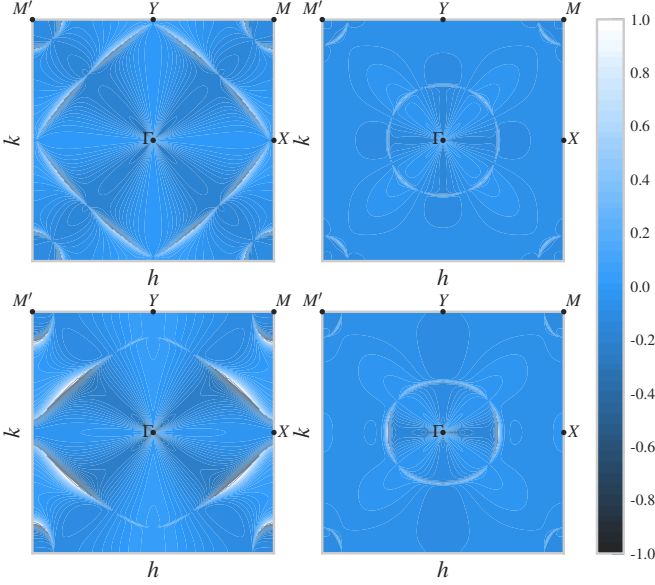


FIG. 7. Contour plots of the difference between renormalized and bare phonon energies $\tilde{\omega}_{m,\vec{q}} - \omega_{m,\vec{q}}$ for the two phonon branches, $m = 1$ (left) and $m = 2$ (right). The upper row shows results for $T = 0.638$ just above the phase transition, while the lower is for $T = 0.604$ just below the phase transition. $(\tilde{g}_1, \tilde{g}_2) = (0.1, 0)$, $J_2 = 1$, $N_x = 256$. In order to perform the subtraction when the lattice gets distorted we set $\vec{q} = h\vec{b}_1 + k\vec{b}_2$ and subtract terms with equal values of (h, k) .

We will focus on the value $J_2 = 1/2$ for which the $J_{\vec{q}}$ minima are at $\vec{q} = \vec{Q}$ such that $6\vec{Q} = \vec{G}$ is a reciprocal lattice vector, corresponding to

$$\vec{Q} \in \pm \frac{\pi}{3} \left\{ \left(0, \frac{2}{\sqrt{3}} \right), \left(1, \frac{1}{\sqrt{3}} \right), \left(-1, \frac{1}{\sqrt{3}} \right) \right\}. \quad (31)$$

Attaching springs with force constants α between nearest neighbors on the triangular lattice gives the dynamical matrix for in-plane phonons

$$\begin{aligned} D_{\vec{k}}^{xx} &= \frac{\alpha}{M} \left(3 - 2 \cos k_x - \cos \frac{k_x}{2} \cos \frac{\sqrt{3}k_y}{2} \right), \\ D_{\vec{k}}^{yy} &= \frac{\alpha}{M} 3 \left(1 - \cos \frac{k_x}{2} \cos \frac{\sqrt{3}k_y}{2} \right), \\ D_{\vec{k}}^{xy} &= \frac{\alpha}{M} \sqrt{3} \sin \frac{k_x}{2} \sin \frac{\sqrt{3}k_y}{2} = D_{\vec{k}}^{yx}. \end{aligned} \quad (32)$$

Note that in contrast to the square lattice, it is not necessary to add next-nearest neighbor springs to ensure stability of the triangular lattice. The elastic modes, ϵ_1 , ϵ_2 , and ϵ_3 , are defined as for the square lattice, but now with corresponding stiffnesses $\mu_1 = 3\alpha/4$, $\mu_2 = 3\alpha/8$ and $\mu_3 = 3\alpha/2$. The corresponding magnetoelastic couplings

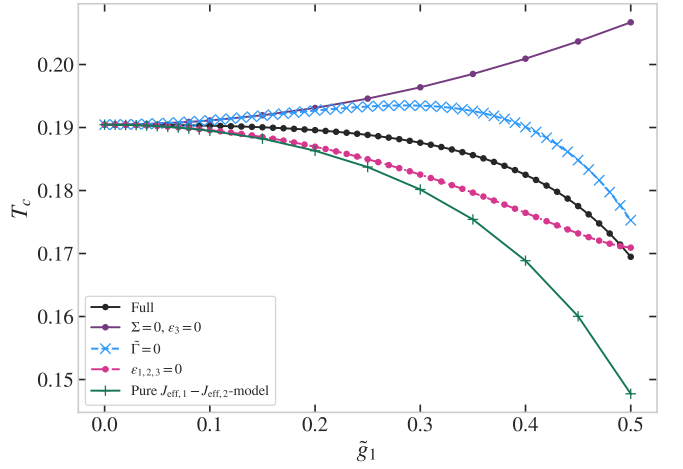


FIG. 8. Critical temperature T_c vs. \tilde{g}_1 for the triangular lattice with $J_1 = -1$ and $J_2 = 0.5$. $L = 240$. The different curves show results obtained under different conditions imposed on the self-consistent equations as indicated by the legends. Full means no extra conditions.

now read

$$\begin{aligned} g_{1,\vec{q}} &= g_1 \frac{1}{\sqrt{2}} \left(\cos q_x - \cos \frac{q_x}{2} \cos \frac{\sqrt{3}q_y}{2} \right), \\ g_{2,\vec{q}} &= -g_1 \frac{\sqrt{3}}{2} \sin \frac{q_x}{2} \sin \frac{\sqrt{3}q_y}{2}, \\ g_{3,\vec{q}} &= g_1 \frac{1}{\sqrt{2}} \left(\cos q_x + 2 \cos \frac{q_x}{2} \cos \frac{\sqrt{3}q_y}{2} \right), \end{aligned} \quad (33)$$

assuming that only the nearest neighbor exchange coupling depends on distance.

For the triangular lattice, already for the system with zero magnetoelastic couplings we find a discontinuous phase transition at $T_c \simeq 0.1905$, with a discontinuity which approaches $\Delta S/N = -0.022$ in the infinite size limit. We find that the first order nature of the phase transition persists also at finite values of \tilde{g}_1 with only minute changes in $\Delta S/N$.

As displayed for the square lattice in Fig. 3, we show in Fig. 8 how T_c changes in the triangular lattice as the strength of the magnetoelastic coupling is increased (black circles). Note that since convergence is better on the triangular lattice for the selected exchange couplings, this plot allows us to explore much larger values than for the square lattice. As for the square lattice, T_c stays almost constant before it clearly decreases for larger values of \tilde{g}_1 . To investigate this we have repeated our analysis where we solve the self-consistent equations under different simplified conditions. In contrast to the symmetry breaking pattern on the square lattice, which only couples to ϵ_1 and not ϵ_2 , the three-fold symmetry breaking on the triangular lattice involves both ϵ_1 and ϵ_2 . As for the square lattice, the purple ($\Sigma = \epsilon_3 = 0$) and the blue (no phonons, $\tilde{\Gamma} = 0$) points agree on a quadratic increase up

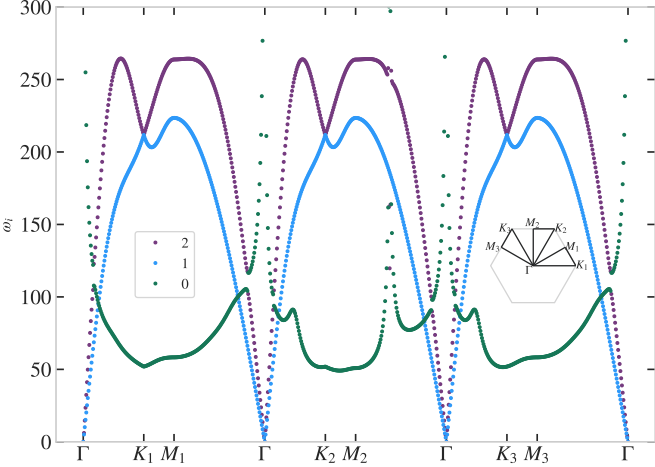


FIG. 9. The renormalized spectra $\tilde{\omega}_{m,\vec{q}}$ for different m values indicated by the legends. The spectra are obtained for $\tilde{g}_1 = 0.4$ and $N_x = 240$, at $T = 0.604$ just below the phase transition, and they are plotted along the Brillouin zone path shown in the right inset.

to roughly $\tilde{g}_1 \approx 0.15$, beyond where they depart rapidly. As for the square lattice, the clamped system (pink circles) exhibits an initial downturn in T_c , which however levels off at larger values of \tilde{g}_1 , which were not available for the square lattice. Even though it leads to a decrease in T_c , phonons are therefore not able to explain the main downturn of the full solution (black circles). Altogether, this indicates that it is the volumetric strain, ϵ_3 , rather than the phonons, which leads to the main decrease in T_c for large \tilde{g}_1 . To confirm this, we once again extracted the ϵ_3 values for the fully coupled system at a temperature just above T_c and computed the effective exchange coupling as $J_{\text{eff},1} = J_1 + g_1 \epsilon_3 / \sqrt{2}$, which was then inserted into the numerically obtained function for T_c from the pure J_1 - J_2 model, $T_c = |J_1| f_{\Delta}(J_2/|J_1|)$. The resulting curve (green pluses) clearly shows the same trend at the largest values of \tilde{g}_1 as the other cases with finite ϵ_3 (black and blue), thus it is reasonable to attribute the main T_c downturn at the largest \tilde{g}_1 to the sensitivity of the pure J_1 - J_2 model towards a stronger value of J_1 which arises because of the uniform contraction of the lattice.

Finally we investigate how the nematic ordering affects the phonon spectrum for the triangular lattice. Fig. 9 shows the renormalized spectra along three symmetry equivalent paths in the Brillouin zone that would be identical if the three-fold nematic symmetry was not broken. The figure is obtained for a temperature just below the phase transition and the $m = 0$ component clearly reveals a lack of symmetry. As for the square lattice the effect on the phonon spectra is generally weak, except for a very narrow patch on the line from the M -points to Γ where the $m = 2$ phonon mode (purple) is radically softened. These momentum space locations, like for example $\pm(0, 2.27)$, are reasonably close to the momentum vectors, $\pm 2\vec{Q} \approx (0, 2.42)$, which connect the two broken

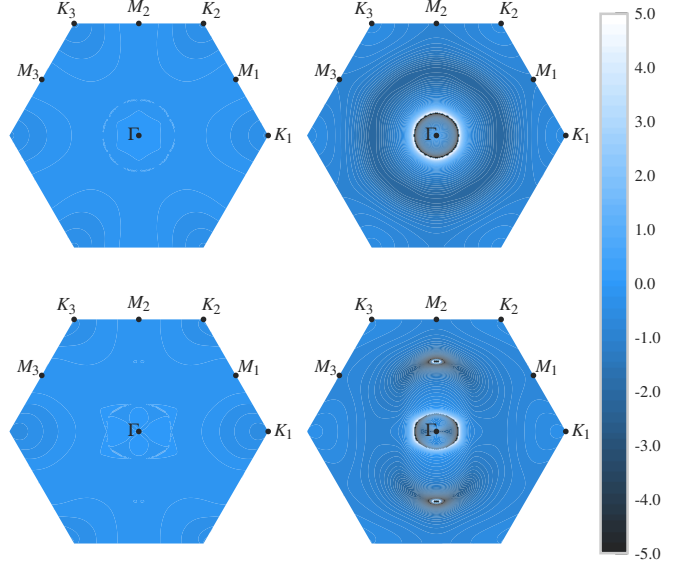


FIG. 10. Contour plots of the difference between renormalized and bare phonon energies $\tilde{\omega}_{m,\vec{q}} - \omega_{m,\vec{q}}$ for the two phonon branches, $m = 1$ (left) and $m = 2$ (right). The upper row shows results for $T = 0.203$ just above the phase transition, while the lower is for $T = 0.172$ just below the phase transition. $N_x = 240$.

symmetry selected minima of $J_{\vec{q}}$.

In Fig. 10 we have plotted the difference of the renormalized and bare phonon spectra for the two phonon modes. In order to enlarge other features than the aforementioned large phonon softening close to $2\vec{Q}$ we have only plotted contours in a narrow region about 0. The effects on the phonon mode 1 is weak, but for phonon mode 2 one can see that the nematic symmetry breaking affects the phonons mainly in two regions encircling the Γ -point. In the circular region closest to the Γ -point there is softening of the phonon frequencies just inside and stiffening just outside. For temperatures below T_c the nematic order imprints its asymmetry on the phonon spectra, and one can clearly see large distortions of the circular regions.

III. DISCUSSION

We have investigated the effects of a weak magnetoelastic coupling on the finite-temperature nematic phase transition displayed by the paradigmatic frustrated two-dimensional J_1 - J_2 Heisenberg model. For both the square, and the triangular lattice, we have found that the coupling to an elastic lattice leads to a nematicostricitive phase transition. We have further analyzed how the magnetoelastic couplings alter the critical temperature of this phase transition, and find a rather complicated picture where several mechanisms together can result in an increase or a decrease of T_c dependent on the specific microscopic details of the system.

For the triangular lattice the transition was found to be discontinuous, regardless of the strength of the magnetoelastic coupling at least up to $\tilde{g}_1 = 0.5$. In contrast, our extrapolations to infinite system size for the square lattice indicate that the transition is continuous for $\tilde{g}_1 < 0.01$, and discontinuous for larger couplings at least up to the largest converged value of $\tilde{g}_1 = 0.15$. Leaving out the phonons, was found to increase the continuous regime, but still resulted in a discontinuous phase transition, hinting that phonons are not essential for understanding the source of the transition becoming discontinuous.

Our results appear to differ from the Monte Carlo results of Ref. [9], which were found to be consistent with a continuous transition. Nevertheless, the magnetoelastic couplings considered there, $\tilde{g}_1 \sim 0.5 - 1.5$, were much larger than what we have managed to get convergence for here for the square lattice. The two results are therefore not necessarily inconsistent, but would appear to indicate an intermediate coupling regime for which the nematostrictive transition is discontinuous.

The fact that a magnetoelastic coupling may cause an otherwise continuous phase transition to become discontinuous was suggested already in Refs. 13 and 14 and later reassessed in more realistic models [6, 7, 15–20]. In essence, the discontinuous nature of the transition arises from a sufficiently large discontinuity in the specific heat at the otherwise continuous transition for the clamped system. Since the NBT approach does not provide an effective theory for the local nematic order parameter, we cannot retrace the argument made in Ref. 15. Nevertheless, one may still gain some insight by considering the effective Landau theory for the homogeneous nematic order parameter. This simplistic mean-field approach, leaving out phonons altogether, is similar to that taken in Ref. 21 to show that ferromagnetic ordering may become discontinuous on a compressible lattice.

From a Landau theory perspective, the C_{4v} symmetry of the square lattice allows for a nematoelastic Gibbs free energy per lattice site at zero pressure of the form

$$\begin{aligned} G/N &= a(T - T_{c,0})O_N^2 + u_4 O_N^4 - \Delta \\ &+ \frac{1}{2}\mu_n\epsilon_n^2 + \frac{N_s}{2N\beta} \sum_{\vec{q}} \ln [\beta(J_{\vec{q}} + \Delta + g_{3,\vec{q}}\epsilon_3)] \\ &+ \eta\epsilon_3 O_N^2 + \lambda\epsilon_1 O_N + \zeta\epsilon_1 O_N^3, \end{aligned} \quad (34)$$

including three unspecified symmetry-allowed couplings, η , λ and ζ , which all vanish for vanishing magnetoelastic couplings, $\tilde{g}_{1,2}$. Leaving out the less important shear mode, ϵ_2 , the free energy is minimized by

$$\epsilon_1 = -(\lambda/\mu_1)O_N - (\zeta/\mu_1)O_N^3, \quad (35)$$

$$\epsilon_3 = -(\eta/\mu_3)O_N^2 + G'_0/\mu_3, \quad (36)$$

with the first derivative with respect to ϵ_3 of the exchange part of the free energy (cf. also Eq. (27)),

$$G'_0 = -\frac{N_s}{2N\beta} \sum_{\vec{q}} \frac{g_{3,\vec{q}}}{J_{\vec{q}} + \Delta}, \quad (37)$$

accounting for the *exchange magnetostriction*, i.e. the finite volumetric strain by which the system lowers its total exchange energy, even in the absence of long-range magnetic and nematic order in our two-dimensional system [22, 23]. Disregarding the nematic order by setting $O_N = 0$ in Eq. (36), this volumetric strain is given by $\epsilon_3 \approx G'_0/\mu_3$, which is negative and therefore corresponds to an isotropic compression of the crystal. This is consistent with the green line in Fig. 4 and already the SCGA ($\Sigma_{\vec{q}} = 0$) captures very well the non-monotonous temperature dependence displayed in the inset, taking its largest absolute value near T_c and vanishing as T and T^{-1} , respectively, for low and high temperatures.

Using Eqs. (35) and (36) to eliminate the strain from Eq. (34), one arrives at the following effective nematic Landau theory

$$\begin{aligned} G_{\min}/N &\approx -\Delta - (G'_0)^2/(2\mu_3) \\ &+ [a(T - T_{c,0}) - \lambda^2/(2\mu_1) + \eta G'_0/\mu_3] O_N^2 \\ &+ [u_4 - \lambda\zeta/\mu_1 - \eta^2/(2\mu_3)] O_N^4, \end{aligned} \quad (38)$$

when retaining at most the quartic term. For small enough couplings, the coefficient of the quartic term in Eq. (38), $u_4 - \lambda\zeta/\mu_1 - \eta^2/(2\mu_3)$, is positive and the nematostrictive transition remains continuous albeit with a renormalized critical temperature given by

$$T_c = T_{c,0} + \lambda^2/(2a\mu_1) - \eta G'_0/(a\mu_3). \quad (39)$$

For large enough couplings, the coefficient of the quartic term may become negative,

$$u_4 - \lambda\zeta/\mu_1 - \eta^2/(2\mu_3) < 0, \quad (40)$$

unless $\lambda\zeta$ becomes negative and overcomes the reduction from the η^2 term. This would imply a discontinuous nematostrictive transition, given that a term of order O_N^6 will be present with a positive coefficient to stabilize the system. Increasing the magnetoelastic coupling further, the couplings η , λ and ζ may depend on $\tilde{g}_{1,2}$ in a non-linear manner, which might break with the criterion (40) and cause the transition to revert back to the continuous nature found in Ref. [9]. This remains speculative, however, since our microscopic NBT calculations do not converge when the magnetoelastic coupling becomes too large.

Although the effects of $Y_{m,\vec{q}}$, i.e. phonons and local constraints, are completely left out, these simple Landau theory considerations for a homogeneous order parameter including strain provide a plausible scenario for why the nematostrictive transition on a square lattice becomes discontinuous above a certain magnitude of the magnetoelastic coupling. Within this simplified description, the specific heat discontinuity for the nematic transition in the clamped system is simply $\Delta C_V = a^2 T_{c,0}/(2u_4)$. Coupling only to the volumetric strain ($\lambda = \zeta = 0$), the criterion (40) may therefore be formulated as

$$\mu_3 < \frac{\Delta C_V}{T_{c,0}} \frac{\eta^2}{a^2} = \frac{2\Delta C_V}{T_{c,0}} \left(\frac{\partial T_{c,0}^*}{\partial \ln V} \right)^2, \quad (41)$$

expressed in physical terms via the volume (i.e. ϵ_3) dependent critical temperature, $T_{c,0}^*(\epsilon_3) = T_{c,0}^* - (\eta/a)\epsilon_3$, inferred from Eq. (34). This criterion is consistent with Ref. 15 (cf. also Refs. 6 and 20), except that there the system was three-dimensional and phonons were included in the analysis, causing μ_3 to be replaced by a different combination of bulk and shear modulus, which diverges with vanishing shear modulus.

Considering the bilinear coupling, λ , by itself ($\eta = \zeta = 0$), the quadratic terms in Eq. (34) are minimized by $O_N = -(\lambda/2a(T - T_{c,0}))\epsilon_1$, which implies a softening of the orthorhombic stiffness to $\mu_1 - \lambda^2/(2a(T - T_{c,0}))$, reaching zero and signaling a joint nematicostrictive transition at $T = T_{c,0} + \lambda^2/(2a\mu_1)$. This scenario is known to impede the nematic fluctuations and lower the critical dimension [4, 5, 16], leading to a smaller discontinuity in the specific heat. When this mechanism dominates the effects of η , one might therefore expect the resulting ΔC_V to become too small for the criterion (41) to be satisfied, resulting in a continuous transition.

As our numerical NBT results suggest, the magnetoelastic coupling to both volumetric and orthorhombic strain, including the corresponding phonon modes, leads

to a complex competition between different effects. Even at the level of Landau theory, these joint effects pose an interesting question for a full renormalization group analysis along the lines of Refs. 4 and 19. Likewise, it should be interesting to study this competition in the quantum critical scenarios studied in Refs. 6 and 7.

IV. ACKNOWLEDGMENTS

We acknowledge useful discussions with Morten Holm Christensen. O.F.S thanks the Niels Bohr Institute Foundation for financial support, and the Condensed Matter Theory group at the Niels Bohr Institute for hospitality. The computations were performed on resources provided by Sigma2 - the National Infrastructure for High Performance Computing and Data Storage in Norway, and on the Fox supercomputer at the University of Oslo.

V. DATA AVAILABILITY

The numerical data are openly available[24].

- [1] P. Chandra, P. Coleman, and A. I. Larkin, Ising transition in frustrated heisenberg models, *Phys. Rev. Lett.* **64**, 88 (1990).
- [2] C. Weber, L. Capriotti, G. Misguich, F. Becca, M. Elhajal, and F. Mila, Ising Transition Driven by Frustration in a 2D Classical Model with Continuous Symmetry, *Phys. Rev. Lett.* **91**, 177202 (2003).
- [3] M. Zacharias, I. Paul, and M. Garst, Quantum Critical Elasticity, *Phys. Rev. Lett.* **115**, 025703 (2015).
- [4] U. Karahasanovic and J. Schmalian, Elastic coupling and spin-driven nematicity in iron-based superconductors, *Phys. Rev. B* **93**, 064520 (2016).
- [5] I. Paul and M. Garst, Lattice Effects on Nematic Quantum Criticality in Metals, *Phys. Rev. Lett.* **118**, 227601 (2017).
- [6] P. Chandra, P. Coleman, M. A. Continentino, and G. G. Lonzarich, Quantum annealed criticality: A scaling description, *Phys. Rev. Res.* **2**, 043440 (2020).
- [7] S. Sarkar, L. Franke, N. Grivas, and M. Garst, Quantum criticality on a compressible lattice, *Phys. Rev. B* **108**, 235126 (2023).
- [8] M. H. Christensen, M. Schütt, A. Klein, and R. M. Fernandes, Microscopic origin of the nematicoelastic coupling and dynamics of hybridized collective nematic-phonon excitations, *Phys. Rev. Res.* **7**, 033298 (2025).
- [9] C. Weber, F. Becca, and F. Mila, Finite-temperature properties of frustrated classical spins coupled to the lattice, *Phys. Rev. B* **72**, 024449 (2005).
- [10] M. Schecter, O. F. Syljuåsen, and J. Paaske, Nematic bond theory of heisenberg helimagnets, *Phys. Rev. Lett.* **119**, 157202 (2017).
- [11] J. T. Chalker, Spin liquids and frustrated magnetism, OUP Academic (2017).
- [12] Glittum, Cecilie and Syljuåsen, Olav F., Arc-shaped structure factor in the $J_1-J_2-J_3$ classical Heisenberg model on the triangular lattice, *Phys. Rev. B* **104**, 184427 (2021).
- [13] O. K. Rice, Thermodynamics of phase transitions in compressible solid lattices, *The Journal of Chemical Physics* **22**, 1535 (1954).
- [14] C. Domb, Specific heats of compressible lattices and the theory of melting, *The Journal of Chemical Physics* **25**, 783 (1956).
- [15] A. Larkin and S. Pikin, Phase transitions of first order but nearly of second, *Soviet Physics JETP* **29**, 891 (1969).
- [16] A. P. Levanyuk and A. A. Sobyanin, Second-order phase transitions without divergences in the second derivatives of the thermodynamic potential, *JETP Letters* **11**, 540 (1970), english translation of *Zh. Éksp. Teor. Fiz., Pis'ma Red.* **11**, 540 (1970).
- [17] J. Sak, Critical behavior of compressible magnets, *Phys. Rev. B* **10**, 3957 (1974).
- [18] F. J. Wegner, Magnetic phase transitions on elastic isotropic lattices, *J. Phys. C: Solid State Phys.* **7**, 2109 (1974).
- [19] D. J. Bergman and B. I. Halperin, Critical behavior of an Ising model on a cubic compressible lattice, *Phys. Rev. B* **13**, 2145 (1976).
- [20] S. A. Pikin, Weak first-order phase transitions, *Physica A* **194**, 352 (1993).
- [21] C. P. Bean and D. S. Rodbell, Magnetic Disorder as a First-Order Phase Transformation, *Phys. Rev.* **126**, 104 (1962).
- [22] R. D. Yacovitch, Y. Shapira, S. Foner, and E. J. McNiff, Exchange magnetostriction in the paramagnetic phase of EuS, *J. Appl. Phys.* **50**, 1677 (1979).

- [23] E. Callen and H. B. Callen, Magnetostriction, Forced Magnetostriction, and Anomalous Thermal Expansion in Ferromagnets, *Phys. Rev.* **139**, A455 (1965).
- [24] O. F. Syljuåsen and J. Paaske, Two-dimensional nematicstrictive phase transitions, 10.5281/zenodo.18507323 (2026).